Article

Saliency-Based Rotor Spatial Position Displacement Self-Sensing for Self-Bearing Machines

Ye gu Kang [1],*, Daniel Fernandez [2] and David Diaz Reigosa [2]

1   School of Electrical, Electronics and Communication Engineering, Koreatech University,
    Chunan-si 31253, Republic of Korea
2   Electrical, Electronic, Computers and Systems Engineering, University of Oviedo, 33204 Oviedo, Spain
*   Correspondence: kang@koreatech.ac.kr

Abstract: Self-bearing machines do not contain physical bearings but magnetic bearings. Both rotor rotary and spatial positions displacement are required in these types of machines to control the rotor position while it is levitating. Self-bearing machines often use external sensors for x (horizontal) and y (vertical) spatial position measurement, which will result in additional cost, volume, complexity, and number of parts susceptible to failure. To overcome these issues, this paper proposes a xy-position estimation self-sensing technique based on both main- and cross-inductance variation. The proposed method estimates x and y position based on inductive saliency between two sets of three-phase coils. The proposed idea is applied on a combined winding self-bearing machine which does not require additional suspension force winding. No additional search coil placement for xy-position estimation is required. Therefore, the proposed algorithm can result in a compact size self-bearing machine that does not require external sensors for xy-position measurement and suspension force winding.

1. Introduction

Conventional rotary machines only allow movement in one degree of freedom (DOF) typically in a rotation axis, i.e., θ_r, shown in Figure 1. Self-bearing machines (bearingless machines), which do not have physical bearings, require controlling spatial xy-position of the rotor in Figure 1 (i.e., xy; x- and y-axes being horizontal and vertical axes) [1]. The remaining axes of the rotor could be controlled actively by a combination of more than two cascade-connected self-bearing machines, or passively by using reluctance forces [2–4].

Conventional self-bearing machines typically comprise two sets of independent windings in the stator for producing torque and suspension force, i.e., separated winding (a torque winding and a suspension winding). For compact size self-bearing machines, combined winding that uses the same coils to create both suspension forces and torque current have been developed [5,6].

Position sensors for closed-loop rotor spatial (xy) position control can be classified into: eddy current based [1,7,8], Hall effect based [9], and optical based sensors [10]. All these sensors result in additional cost, volume, complexity, and number of parts susceptible to failure [10,11]. In [12], model reference adaptive system (MRAS) is proposed to enable position self-sensing in a high speed region. In a zero-to-low speed region, high-frequency injection (HFI) has been demonstrated to be a viable option for xy-position estimation both in magnetic bearings [13–16] and self-bearing machines [17–20]. However, previously published HFI techniques applied to self-bearing machines are limited to: (i) In [17,18], separated winding machines utilizing suspension force windings mutual coupling inductances are proposed; (ii) In [19,20], separate search coils are installed to reduce input signal noise

level by enabling differential mode for spatial rotor position estimation. In [20], search coil placement arrangement is investigated for minimizing the unwanted influence between suspension windings and pulse-width modulation (PWM) noise. It can be concluded that the previously proposed HFI techniques in the literature require additional windings or hardware which will result in increasing system volume and cost. Table 1 summarizes the existing HFI position self-sensing technique for self-bearing machines.
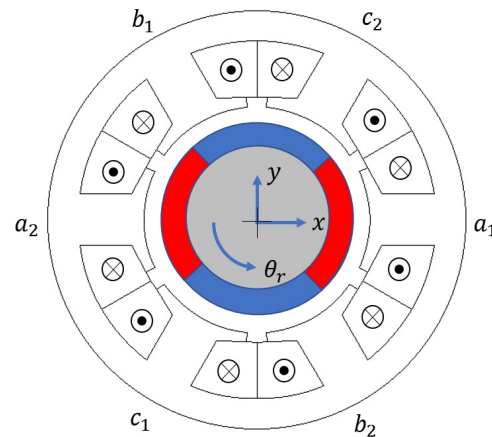

Figure 1. Four-pole, six-slot, combined winding self-bearing machine.

Table 1. HFI spatial position self-sensing methods comparison.

	Methodology		
	Input Signal Mode	**Require Additional Winding**	**Winding Type**
[17,18]	Common	No	Separated
[19,20]	Differential	Yes [1]	Separated
Proposed	Differential	No	Combined

[1] Additional hardware placement is required.

This paper proposes an HFI based xy-rotor position self-sensing technique for combined winding machines, therefore, achieving a compact size self-bearing system minimizing cost, volume, and reliability issues since it does not require additional winding or hardware. The combined winding machine has each phase connected to an inverter terminal that carries both suspension force and torque current. The target self-bearing machine winding is classified as multi-phase (MP), which has two sets of three-phase winding with two neutral points as in Figure 2 to enable dual field-oriented control for independent torque and force control [6,21]. The high-frequency (HF) signal will be injected in both sets of three-phase coils to enable use of differential mode input for xy-position estimation in a stationary reference frame. It will be shown that main- and cross-inductances variation depend on the rotor x- and y-positions, respectively, which will enable xy-position estimation self-sensing. The proposed HFI based self-sensing technique will be evaluated on a combined winding, 4-pole, 6-slot surface permanent magnet bearingless synchronous machine (SPMBSM).

The paper is organized as follows: HF voltage model of the target BPMSM for xy-position self-sensing is developed in Section 2. Section 3 introduces an analytical model that relates inductive saliency and rotor xy-position displacement. Section 4 presents the xy-position self-sensing method and its implementation. Section 5 presents experimental results; Finally, in Section 6, conclusions are drawn.
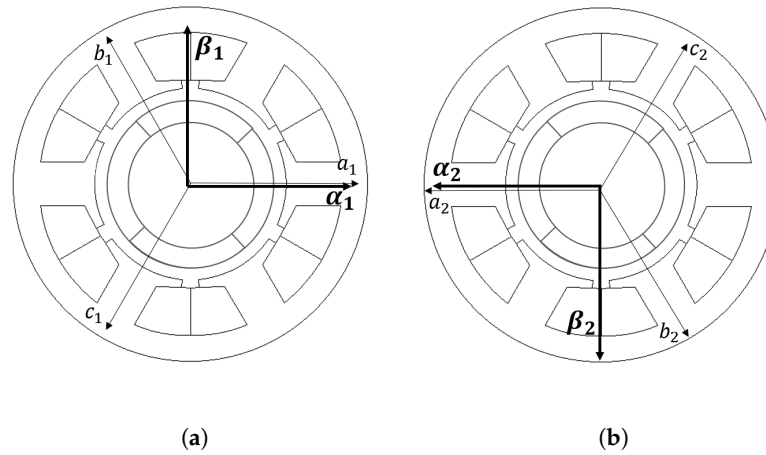
Figure 2. *abc* to $\alpha\beta$ transformations: (**a**) a_1, b_1, c_1, and α_1, β_1; (**b**) a_2, b_2, c_2, and α_2, β_2.

2. High-Frequency Model of a Self-Bearing Machine

The self-bearing machine voltage characteristic model is presented in this section. The inductive saliency model as a function of x and y displacement, later, will be used for the proposed self-sensing algorithm. The 4-pole, 6-slot combined winding self-bearing machine shown in Figure 1 will be used in this paper. Both the stator and the rotor core are soft magnetic material. The machine has two sets of three-phase windings (a_1, b_1, c_1, and a_2, b_2, c_2) with separated neutral points to control direction of flux induced from armature current. The two sets of three-phase windings are placed 180° mechanical angle apart from each other:

$$v_{an} = R_p i_{an} + \frac{d\lambda_{an}}{dt} \tag{1}$$

$$
\begin{aligned}
v_{an} = {}& R_p i_{an} + L_{anan}(x,y)\frac{di_{an}}{dt} + L_{anbn}(x,y)\frac{di_{bn}}{dt} \\
& + L_{ancn}(x,y)\frac{di_{cn}}{dt} + L_{anam}(x,y)\frac{di_{am}}{dt} + L_{anbm}(x,y)\frac{di_{bm}}{dt} \\
& + L_{ancm}(x,y)\frac{di_{cm}}{dt} + k_{e\theta_r an}(x,y)\frac{d\theta_r}{dt} + k_{exan}(x,y)\frac{dx}{dt} \\
& + k_{eyan}(x,y)\frac{dy}{dt}
\end{aligned}
\tag{2}
$$

2.1. Phase Voltage Model

Phase a_n voltage characteristic model is shown in (1), where R_p, v_{an}, i_{an}, and λ_{an} represent phase resistance, phase voltage, current, and flux linkage, respectively. n and m represent the first and the second sets of three-phase coils in Figure 2. Phase a_n voltage characteristic equation can also be expressed by (2), where L_{anan} is self-inductance, L_{anbn} and L_{ancn} represent mutual-inductances, L_{anam}, L_{anbm}, L_{ancm}, are cross-coupling inductance between coil sets n and m. $k_{e\theta_r an}$, k_{exan}, and k_{eyan} are back-EMF variables with respect to θ_r-, x-, and y-position movement [1,9]. Note that the self- and mutual-inductances vary when the rotor spatial position (x, y) change. This is due to the unbalanced air-gap length between phases [22].

2.2. $\alpha\beta_n$-Axes Voltage Model

Six-phase voltage models can be presented as two sets of $\alpha\beta_n$-axes (4) and (5). When n is equal to 1, m is equal to 2, and vice versa. Clark transform, K_c, in (3) is used.

$$\begin{bmatrix} \alpha_n \\ \beta_n \end{bmatrix} = \frac{2}{3} \begin{bmatrix} 1 & -0.5 & -0.5 \\ 0 & \frac{\sqrt{3}}{2} & -\frac{\sqrt{3}}{2} \end{bmatrix} \begin{bmatrix} a_n \\ b_n \\ c_n \end{bmatrix} = K_c \begin{bmatrix} a_n \\ b_n \\ c_n \end{bmatrix} \quad (3)$$

$$
\begin{aligned}
v_{\alpha n} =\ & R_p i_{\alpha n} + L_{\alpha n \alpha n}(x,y)\frac{di_{\alpha n}}{dt} + L_{\alpha n \beta n}(x,y)\frac{di_{\beta n}}{dt} \\
& + L_{\alpha n \alpha m}(x,y)\frac{di_{\alpha m}}{dt} + L_{\alpha n \beta m}(x,y)\frac{di_{\beta m}}{dt} \\
& + k_{e\theta_r \alpha n}(x,y)\frac{d\theta_r}{dt} + k_{ex\alpha n}(x,y)\frac{dx}{dt} + k_{ey\alpha n}(x,y)\frac{dy}{dt}
\end{aligned}
\quad (4)
$$

$$
\begin{aligned}
v_{\beta n} =\ & R_p i_{\beta n} + L_{\beta n \beta n}(x,y)\frac{di_{\beta n}}{dt} + L_{\beta n \alpha n}(x,y)\frac{di_{\alpha n}}{dt} \\
& + L_{\beta n \beta m}(x,y)\frac{di_{\beta m}}{dt} + L_{\beta n \alpha m}(x,y)\frac{di_{\alpha m}}{dt} \\
& + k_{e\theta_r \beta n}(x,y)\frac{d\theta_r}{dt} + k_{ex\beta n}(x,y)\frac{dx}{dt} + k_{ey\beta n}(x,y)\frac{dy}{dt}
\end{aligned}
\quad (5)
$$

2.3. High-Frequency Voltage Model

The HF voltage characteristic model in stationary reference frame is represented by (6) and (7), obtained from (4) and (5) after neglecting the resistance terms, eliminating back-EMF terms, and cross-coupling inductances between three-phase coil sets. If the frequency of the HF signal feeding the machine is sufficiently high, the resistive terms can be safely neglected as the inductive terms dominate the machine impedance. The back-EMF term can also be eliminated as it does not contain HF component. The cross-coupling inductance between three-phase coil sets are small and insensitive to xy-position variation (see Figure 3).
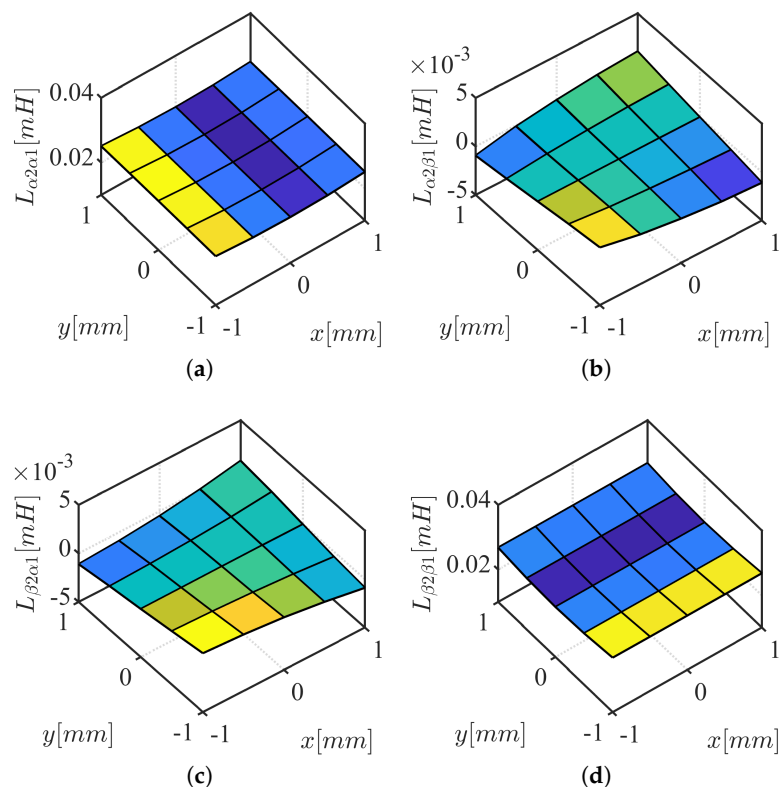

Figure 3. $\alpha\beta_2$ three-phase cross-coupling inductance results from FEA: (**a**) $L_{\alpha 2\alpha 1}$; (**b**) $L_{\alpha 2\beta 1}$; (**c**) $L_{\beta 2\alpha 1}$; (**d**) $L_{\beta 2\beta 1}$.

It will be shown in Section 3 that $L_{\alpha n \alpha n}$, $L_{\beta n \beta n}$, $L_{\alpha n \beta n}$, and $L_{\beta n \alpha n}$ are a function of the *x*- and *y*-spatial rotor position displacement. This dependency will be used for rotor *xy*-position estimation:

$$v_{\alpha n HF} = L_{\alpha n \alpha n}(x,y)\frac{di_{\alpha n}}{dt} + L_{\alpha n \beta n}(x,y)\frac{di_{\beta n}}{dt} \tag{6}$$

$$v_{\beta n HF} = L_{\beta n \beta n}(x,y)\frac{di_{\beta n}}{dt} + L_{\beta n \alpha n}(x,y)\frac{di_{\alpha n}}{dt} \tag{7}$$

Finally, since $\alpha\beta_2$ is rotated $180°$ with respect to $\alpha\beta_1$, the relationships shown in (8)–(11) exist among inductances in $\alpha\beta_1$ and $\alpha\beta_2$ reference frames.

$$L_{\alpha 2 \alpha 2}(x,y) = L_{\alpha 1 \alpha 1}(-x,-y) \tag{8}$$

$$L_{\alpha 2 \beta 2}(x,y) = L_{\alpha 1 \beta 1}(-x,-y) \tag{9}$$

$$L_{\beta 2 \beta 2}(x,y) = L_{\beta 1 \beta 1}(-x,-y) \tag{10}$$

$$L_{\beta 2 \alpha 2}(x,y) = L_{\beta 1 \alpha 1}(-x,-y) \tag{11}$$

3. HF Inductance Dependency and Rotor *xy*-Position Displacement

This section presents the inductance dependency in rotor spatial position displacement (i.e., *xy*-position). A simplified air-gap reluctance model is developed for the analysis of the self-bearing machine inductances sensitivity on rotor *xy*-position displacement. The conclusions drawn from the analysis are verified using finite element analysis (FEA).

3.1. Inductance Dependency Analysis Based on Air-Gap Reluctance Model

Equivalent inductance, L_{eq}, is shown in (12) as a function of reluctance, where N_{eq} represents the number of turns. The reluctance in the air-gap is defined by (13), where μ_0, A_{eq}, and l_{eq} are the absolute permeability of the air, equivalent area, and air-gap length, respectively:

$$L_{eq} = \frac{N_{eq}^2}{R} \tag{12}$$

$$R = \frac{l_{eq}}{\mu_0 A_{eq}} \tag{13}$$

Simplified magnetic equivalent circuit of the first set of three-phase coils, abc_1, is developed, assuming the air-gap reluctances are the dominant components in the flux-path. The reluctance components in the flux path of the rotor and stator are negligible and not included in the machine model. Infinite relative permeability of soft-iron is assumed. The relative permeability of PM is set equal to air. The three-phase magnetic circuit is shown in Figure 4, where I_{a1}, I_{b1}, I_{c1}, ϕ_{a1}, ϕ_{b1}, and ϕ_{c1} are abc_1 phase currents and abc_1 fluxes.

The abc_1 phase flux-linkage can be expressed by (21), solving Figure 4 using superposition [23], where phase flux-linkages λ_{a1}, λ_{b1}, and λ_{c1} are obtained from multiplying the number of turns to the phase flux.

The phase flux-linkages in (21) can be expressed in an $\alpha\beta_1$ reference frame as in (22) applying Clark transformation. The HF inductances, $L_{\alpha 1 \alpha 1}$, $L_{\alpha 1 \beta 1}$, $L_{\beta 1 \alpha 1}$, and $L_{\beta 1 \beta 1}$ in (6) and (7) are derived using the phase air-gap reluctances. It is important to note that each phase reluctance is a function of the air-gap length (13). Therefore, if the rotor *xy*-position varies, the HF inductances will vary. The rotor should be designed with the least *dq*-axes inductive saliency to utilize the *xy*-position inductive saliency based on air-gap length variation for *xy*-position self-sensing.
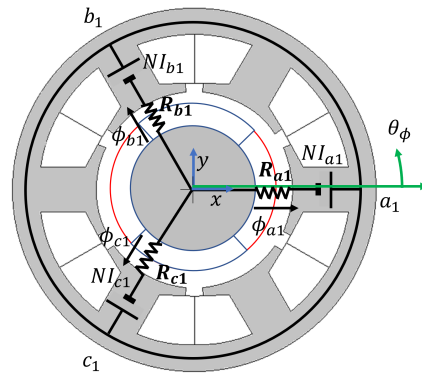
Figure 4. Simplified magnetic equivalent circuit of abc_1 based on air-gap reluctance.

3.2. $\alpha\beta_n$ Inductance Sensitivity Analysis

In this subsection, inductance sensitivity analysis is performed. Air-gap length in each phase is modeled as in (14) using Euler's formula to correlate each phase air-gap length in polar coordinates to the xy-position variation in Cartesian coordinates. θ_ϕ is the angle of the phase reluctance referencing the location of phase $a1$ as in Figure 4. r is the per-unit air-gap length. Δx and Δy are the per-unit rotor displacement in x- and y-axes. The effect of Δx and Δy on two sets of three-phase air-gap is modeled using the relative angle, θ_ϕ, in Table 2.

$$l_{eq} = |r - (\Delta x + j\Delta y)exp(j\theta_\phi)| \tag{14}$$

Table 2. Phase equivalent air-gap length model.

Air-Gap Length	θ_ϕ [rad]	Air-Gap Length	θ_ϕ [rad]
l_{a1}	0	l_{a2}	π
l_{b1}	$2\pi/3$	l_{b2}	$\pi + 2\pi/3$
l_{c1}	$-2\pi/3$	l_{c2}	$\pi - 2\pi/3$

Taking the dominant components, per unit air-gap length is calculated in (15)–(20):

$$l_{a1} = \sqrt{1 - 2\Delta x} \tag{15}$$

$$l_{b1} = \sqrt{1 + \Delta x + \sqrt{3}\Delta y} \tag{16}$$

$$l_{c1} = \sqrt{1 + \Delta x - \sqrt{3}\Delta y} \tag{17}$$

$$l_{a2} = \sqrt{1 + 2\Delta x} \tag{18}$$

$$l_{b2} = \sqrt{1 - \Delta x - \sqrt{3}\Delta y} \tag{19}$$

$$l_{c2} = \sqrt{1 - \Delta x + \sqrt{3}\Delta y} \tag{20}$$

$$\begin{bmatrix} \lambda_{a1} \\ \lambda_{b1} \\ \lambda_{c1} \end{bmatrix} = \begin{bmatrix} N_{eq}\phi_{a1} \\ N_{eq}\phi_{b1} \\ N_{eq}\phi_{c1} \end{bmatrix}$$

$$= \frac{N_{eq}^2}{R_{a1}R_{b1} + R_{a1}R_{c1} + R_{b1}R_{c1}} \begin{bmatrix} (R_{b1} + R_{c1}) & -R_{c1} & -R_{b1} \\ -R_{c1} & (R_{a1} + R_{c1}) & -R_{a1} \\ -R_{b1} & -R_{a1} & (R_{a1} + R_{b1}) \end{bmatrix} \begin{bmatrix} i_{a1} \\ i_{b1} \\ i_{c1} \end{bmatrix} \tag{21}$$

$$\begin{bmatrix} \lambda_{\alpha 1} \\ \lambda_{\beta 1} \end{bmatrix} = \begin{bmatrix} L_{\alpha 1 \alpha 1} & L_{\alpha 1 \beta 1} \\ L_{\beta 1 \alpha 1} & L_{\beta 1 \beta 1} \end{bmatrix} \begin{bmatrix} i_{\alpha 1} \\ i_{\beta 1} \end{bmatrix}$$

$$= \frac{N_{eq}^2}{2(R_{a1}R_{b1} + R_{a1}R_{c1} + R_{b1}R_{c1})} \begin{bmatrix} 3(R_{b1} + R_{c1}) & \sqrt{3}(R_{b1} - R_{c1}) \\ \sqrt{3}(R_{b1} - R_{c1}) & 4R_{a1} + R_{b1} + R_{c1} \end{bmatrix} \begin{bmatrix} i_{\alpha 1} \\ i_{\beta 1} \end{bmatrix} \tag{22}$$

Equivalent air-gap area, A_{eq}, and air-gap permeability are assumed equal for each phase. Substituting the phase reluctance to (22), taking Taylor's series expansion near center position, (23) is calculated as function of x and y rotor position displacement, Δx and Δy. Similarly, the second set of inductances is calculated in (24). The sensitivity analysis based air-gap reluctance is verified using FEA in Figures 5 and 6 in Section 3.2:

$$\begin{bmatrix} L_{\alpha 1 \alpha 1} & L_{\alpha 1 \beta 1} \\ L_{\beta 1 \alpha 1} & L_{\beta 1 \beta 1} \end{bmatrix} = \frac{N_{eq}^2 A_{eq} \mu_0}{2 * 3} \begin{bmatrix} 6 + 3\Delta x & 3\Delta y \\ 3\Delta y & 6 - 3\Delta x \end{bmatrix} \tag{23}$$

$$\begin{bmatrix} L_{\alpha 2 \alpha 2} & L_{\alpha 2 \beta 2} \\ L_{\beta 2 \alpha 2} & L_{\beta 2 \beta 2} \end{bmatrix} = \frac{N_{eq}^2 A_{eq} \mu_0}{2 * 3} \begin{bmatrix} 6 - 3\Delta x & -3\Delta y \\ -3\Delta y & 6 + 3\Delta x \end{bmatrix} \tag{24}$$

The conclusions of inductance variation in x and y rotor position displacement from the simplified inductance model can be summarized as follows:

- Main inductances, $L_{\alpha n \alpha n}$ and $L_{\beta n \beta n}$, are sensitive to x-axis rotor movement. For x-position self-sensing, main inductances are required.
- Cross-coupling inductances, $L_{\alpha n \beta n}$ and $L_{\beta n \alpha n}$, are sensitive to y-axis rotor movement. For y-position self-sensing, cross-coupling inductances are required.
- Cross-coupling inductances, $L_{\alpha n \beta n}$ and $L_{\beta n \alpha n}$, are equal.
- The main and cross-coupling inductances in the first and the second set of three-phase coils have opposite sensitivity to xy-axes rotor movement.
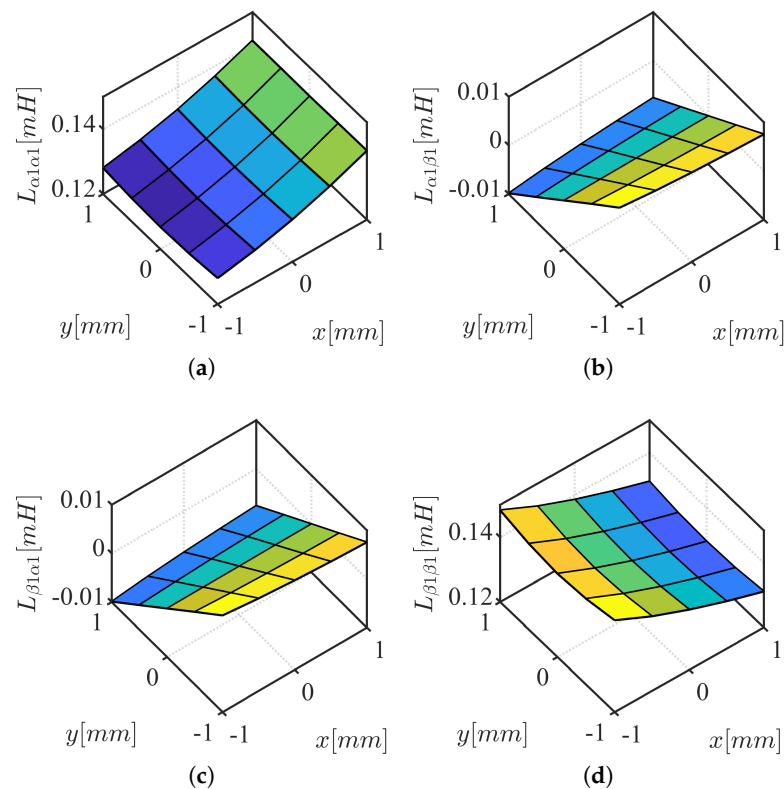

Figure 5. $\alpha \beta_1$ inductance results from FEA: (**a**) $L_{\alpha 1 \alpha 1}$; (**b**) $L_{\alpha 1 \beta 1}$; (**c**) $L_{\beta 1 \alpha 1}$; (**d**) $L_{\beta 1 \beta 1}$.
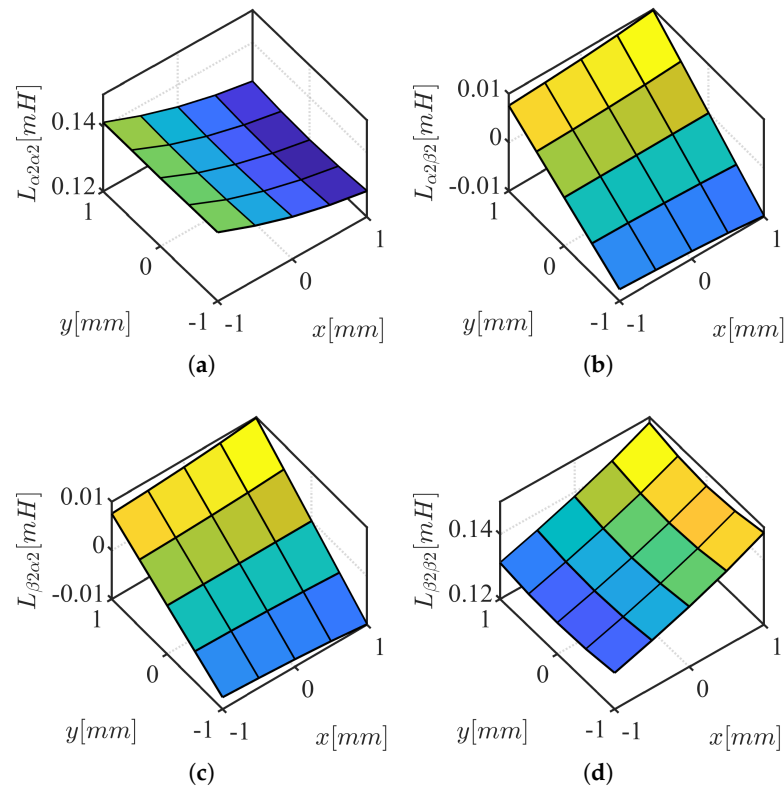
Figure 6. $\alpha\beta_2$ inductance results from FEA: (**a**) $L_{\alpha2\alpha2}$; (**b**) $L_{\alpha2\beta2}$; (**c**) $L_{\beta2\alpha2}$; (**d**) $L_{\beta2\beta2}$.

3.3. Inductance Dependency Verification Using FEA

Two-dimensional static finite element analysis (FEA) is performed to verify the conclusions from the simplified reluctance model. A stacking factor of 0.95 is used for the stator with N35 grade NdFeB permanent magnet on the rotor. Self-bearing machine geometry and simulation conditions for FEA analysis are summarized in Table 3, where D_{os}, D_{is}, D_{or}, w_t, t_{PM}, and L_{st} are stator outer and inner diameter, outer diameter of the rotor, teeth width, thickness of the magnet, and stack length; see Figure 7. 0.2 p.u. of HF current is injected in the first set of three-phase coils, n, while the other set of three-phase coils current, m, are set to zero (25) and (26). Inductances are calculated based on FEA by taking partial derivative of HF flux-linkage with respect to the HF current (27)–(30). Given $n = 1$, $m = 2$, $i = 1$, $j = 1$, main and cross-coupling inductances shown in Figure 5 are calculated for the first set of coil inductances while $n = 2$, $m = 1$, $i = 1$, $j = 1$ calculates the second set of the coil inductance in Figure 6. The trends of inductance variation are matching with analysis based on air-gap reluctances in Section 3.2.
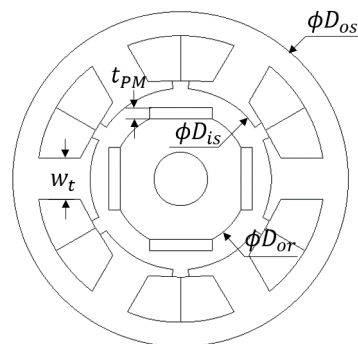

Figure 7. Cross-section of target SPMBSM and relevant geometric variables for FEA.

Table 3. FE analysis conditions and self-bearing machine.

Poles	4	D_{os}	50 [mm]
Slots	6	D_{is}	26.8 [mm]
Turns	16	D_{or}	19.6 [mm]
Permanent magnet	N35	w_t	6 [mm]
Soft material	M-19	t_{PM}	1.4 [mm]
L_{st}	24.5 [mm]	I_{rated}	5 [A]
x_{max}	±2 [mm]	x	−1 to 1 in 0.5 [mm] step
y_{max}	±2 [mm]	y	−1 to 1 in 0.5 [mm] step

The cross-coupling inductance between the first and the second set of three-phase coils, shown in Figure 3, are calculated using $n = 1$, $m = 2$, $i = 1$, $j = 2$. Note that the magnitude of the cross-coupling inductances between three-phase coil sets are much smaller (about 1/5 times) than the self inductances shown in Figures 5 and 6. Moreover, the inductances are not sensitive to xy-position variation. This is because the air-gap reluctance sensitivity of $abc1$ and $abc2$ to xy-position variation are in opposite directions (see Table 2 with angle offset, θ_ϕ, of π between $abc1$ and $abc2$). This is due to the air-gap reluctance sensitivity of $\alpha\beta1$ and $\alpha\beta2$ are in π shifted (opposite) relations (see Table 2). Therefore, the coupling inductances between three-phase coil sets are not included in the xy-position self-sensing model.

$$\begin{bmatrix} i_{\alpha n} \\ i_{\beta n} \end{bmatrix} = K_c \begin{bmatrix} i_{an} \\ i_{bn} \\ i_{cn} \end{bmatrix} \tag{25}$$

$$\begin{bmatrix} i_{\alpha m} \\ i_{\beta m} \end{bmatrix} = \begin{bmatrix} 0 \\ 0 \end{bmatrix} \tag{26}$$

$$L_{\alpha i \alpha j}(x, y) = \frac{\partial \lambda_{\alpha i}(x, y)}{\partial i_{\alpha j}} \tag{27}$$

$$L_{\alpha i \beta j}(x, y) = \frac{\partial \lambda_{\alpha i}(x, y)}{\partial i_{\beta j}} \tag{28}$$

$$L_{\beta i \beta j}(x, y) = \frac{\partial \lambda_{\beta i}(x, y)}{\partial i_{\beta j}} \tag{29}$$

$$L_{\beta i \alpha j}(x, y) = \frac{\partial \lambda_{\beta i}(x, y)}{\partial i_{\alpha j}} \tag{30}$$

4. HFI Based xy-Position Self-Sensing

xy-position estimation based on the injection of an HF signal is presented.

Equations (6) and (7) can be expressed as (31), where s is the differential operator. Park transform in (32) with reference frame offset angle θ_{inj} is defined to rotate the stationary reference frame. Pulsating HF voltages are injected in between $\alpha\beta$-axes (33) where θ_{inj} of 45° is chosen to excite both α- and β-axes simultaneously (as shown in Figure 8) [24]. The same magnitude HF voltage command is used for both sets of three-phase coil set ($n = 1$, $n = 2$) as in (33) to use differential information to enhance position estimation accuracy.

$$\begin{bmatrix} v_{\alpha n HF} \\ v_{\beta n HF} \end{bmatrix} = s \begin{bmatrix} L_{\alpha n \alpha n} & L_{\alpha n \beta n} \\ L_{\beta n \alpha n} & L_{\beta n \beta n} \end{bmatrix} \begin{bmatrix} i_{\alpha n HF} \\ i_{\beta n HF} \end{bmatrix} \tag{31}$$

$$K_p(\theta_{inj}) = \begin{bmatrix} cos(\theta_{inj}) & sin(\theta_{inj}) \\ -sin(\theta_{inj}) & cos(\theta_{inj}) \end{bmatrix} \tag{32}$$

$$\begin{bmatrix} v_{\alpha n HF}^{\theta_{inj}} \\ v_{\beta n HF}^{\theta_{inj}} \end{bmatrix} = V_{HF} cos(2\pi f_{HF} t) \begin{bmatrix} 1 \\ 0 \end{bmatrix} \tag{33}$$

$$\begin{bmatrix} v_{\alpha n HF}^* \\ v_{\beta n HF}^* \end{bmatrix} = K_p(45)^{-1} \begin{bmatrix} v_{\alpha n HF}^{\theta_{inj}} \\ v_{\beta n HF}^{\theta_{inj}} \end{bmatrix} \tag{34}$$

$$\begin{bmatrix} i_{\alpha n HF}^{\theta_{inj}} \\ i_{\beta n HF}^{\theta_{inj}} \end{bmatrix} = K_p(45) \begin{bmatrix} i_{\alpha n HF} \\ i_{\beta n HF} \end{bmatrix}$$

$$= sin(2\pi f_{HF} t) \begin{bmatrix} I_{i0n} \\ I_{i1n} \end{bmatrix} \tag{35}$$

$$\begin{bmatrix} I_{i0n} \\ I_{i1n} \end{bmatrix} = \frac{V_{HF}}{2\pi f_{HF}(L_{\alpha n \alpha n} L_{\beta n \beta n} - L_{\alpha n \beta n} L_{\beta n \alpha n})} \begin{bmatrix} \frac{(L_{\alpha n \alpha n} + L_{\beta n \beta n})}{2} & -\frac{(L_{\alpha n \beta n} + L_{\beta n \alpha n})}{2} \\ -\frac{(L_{\alpha n \alpha n} - L_{\beta n \beta n})}{2} & -\frac{(L_{\alpha n \beta n} - L_{\beta n \alpha n})}{2} \end{bmatrix} \tag{36}$$
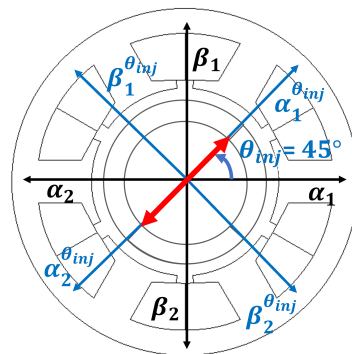

Figure 8. HF pulsating voltage injection reference frame, $\alpha \beta_1^{\theta_{inj}}$ and $\alpha \beta_2^{\theta_{inj}}$ with θ_{inj}, and stationary reference frame, $\alpha \beta_1$ and $\alpha \beta_2$.

V_{HF} and f_{HF} represent the HF voltage magnitude and frequency. f_{HF} should be selected far apart from the controlled torque or force current frequency to minimize the interference. The HF voltage command input in the stationary reference frame will be (34). The resulting stator HF current response will be Park transformed to the HF injection reference frame as in (35), where I_{i0n} and I_{i1n} are injection reference frame HF current magnitude defined in (36).

This question arises: How can this HF current response can be used to estimate x and y rotor position? This may be explained referring to (23), (24), and (36). The main inductances, $L_{\alpha n \alpha n}$ and $L_{\beta n \beta n}$, are proportional to Δx. On the other hand, the cross-coupling inductances, $L_{\alpha n \beta n}$ and $L_{\beta n \alpha n}$, are sensitive to Δy. The inductance term in the denominator of (36), $\frac{V_{HF}}{2\pi f_{HF}} \frac{1}{(L_{\alpha n \alpha n} L_{\beta n \beta n} - L_{\alpha n \beta n} L_{\beta n \alpha n})}$ becomes $\frac{V_{HF}}{2\pi f_{HF}} \frac{36}{(N_{eq} A_{eq} \mu_0)(36 - 9(\Delta x)^2 - 9(\Delta y)^2)}$ since the term is insensitive to small Δx and Δy. N_{eq}, A_{eq}, μ_0, V_{HF}, and f_{HF} are assumed to be constants. Therefore, I_{i0n} and I_{i1n} have the xy-position dependency relationship shown in (37) and (38).

Exciting both $\alpha\beta_1$ and $\alpha\beta_2$ with (33) as in Figure 8, x and y rotor position are estimated, from the HF current responses, (39) and (40). Figure 9 shows FEA based results of differential HF currents in (39) and (40). The definitions of k_{gx} and k_{ox} are shown in Figure 9a, where k_{gx} is x-axis proportional gain for unit conversion from HF current, i.e., amperes (A), to position, e.g., millimeter (mm), given HF injection conditions, i.e., V_{HF}, f_{HF}. k_{ox} is the x-axis offset constant to calibrate the x-axis referencing position. The procedure to select the self-sensing gains is as follows:

- first, k_{gx} and k_{gy} are set to 1 while searching for the values of k_{ox} and k_{oy} that will result in $\hat{x} = \hat{y} = 0$ in (39) and (40) at the rotor position $x = y = 0$ mm. k_{ox} and k_{oy} are non-zero values if the two sets of three-phase are not in perfect symmetry.
- second, k_{gx} and k_{gy} are selected to convert the estimated position unit to the unit in millimeters.

$$\begin{bmatrix} I_{i01} \\ I_{i11} \end{bmatrix} \approx \begin{bmatrix} \frac{(L_{\alpha1\alpha1}+L_{\beta1\beta1})}{2} & -\frac{(L_{\alpha1\beta1}+L_{\beta1\alpha1})}{2} \\ -\frac{(L_{\alpha1\alpha1}-L_{\beta1\beta1})}{2} & -\frac{(L_{\alpha1\beta1}-L_{\beta1\alpha1})}{2} \end{bmatrix}$$
$$\propto \begin{bmatrix} \frac{(\Delta x - \Delta x)}{2} & -\frac{(\Delta y + \Delta y)}{2} \\ -\frac{(\Delta x + \Delta x)}{2} & -\frac{(\Delta y - \Delta y)}{2} \end{bmatrix} = \begin{bmatrix} -\Delta y \\ -\Delta x \end{bmatrix} \tag{37}$$

$$\begin{bmatrix} I_{i02} \\ I_{i12} \end{bmatrix} \approx \begin{bmatrix} \frac{(L_{\alpha2\alpha2}+L_{\beta2\beta2})}{2} & -\frac{(L_{\alpha2\beta2}-L_{\beta2\alpha2})}{2} \\ -\frac{(L_{\alpha2\alpha2}-L_{\beta2\beta2})}{2} & -\frac{(L_{\alpha2\beta2}-L_{\beta2\alpha2})}{2} \end{bmatrix}$$
$$\propto \begin{bmatrix} \frac{(-\Delta x + \Delta x)}{2} & -\frac{(-\Delta y - \Delta y)}{2} \\ -\frac{(-\Delta x - \Delta x)}{2} & -\frac{(-\Delta y + \Delta y)}{2} \end{bmatrix} = \begin{bmatrix} \Delta y \\ \Delta x \end{bmatrix} \tag{38}$$

$$\hat{x} = k_{gx}((I_{i12} - I_{i11}) + k_{ox}) \tag{39}$$
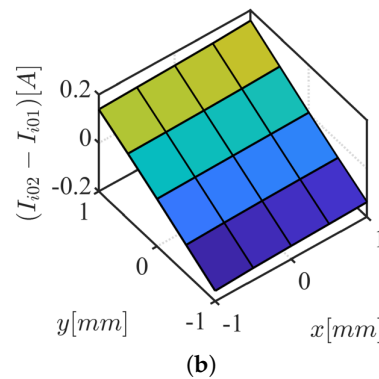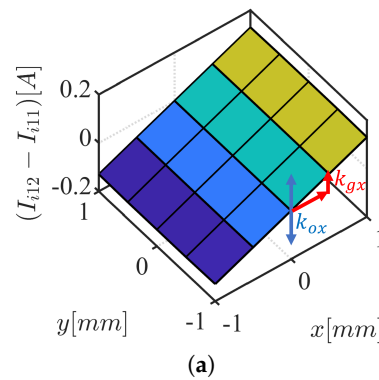$$\hat{y} = k_{gy}((I_{i02} - I_{i01}) + k_{oy}) \tag{40}$$

(**a**)

(**b**)

Figure 9. FEA results of differential HF currents, $V_{HF} = 1$ V, $f_{HF} = 1000$ Hz, and gain and offset constant, k_{gx} and k_{ox}. (**a**) ($I_{i12} - I_{i11}$); (**b**) ($I_{i02} - I_{i01}$).

xy-Position Self-Sensing Implementation

Figure 10 presents the overall *xy*-position self-sensing block diagram. An HF pulsating voltage is injected in 45° injection reference frame, i.e., in between $\alpha\beta_1$ and $\alpha\beta_2$ as shown in Figure 8. The commanded HF voltages are input into a self-bearing machine in (6) and (7) using a PWM voltage source inverter (VSI). Two sets of three-phase current responses are measured using 6-current transducers and Clark transformed. HF current responses, I_{i0n} and I_{i1n} containing *xy*-position information, are rotated back to $\alpha\beta_1$ and $\alpha\beta_2$ reference frame. The HF current is demodulated with a low pass filter (LPF) after multiplying HF current with sine wave at injected frequency, f_{HF}. Finally, *x* and *y* rotor positions are estimated using (39) and (40).
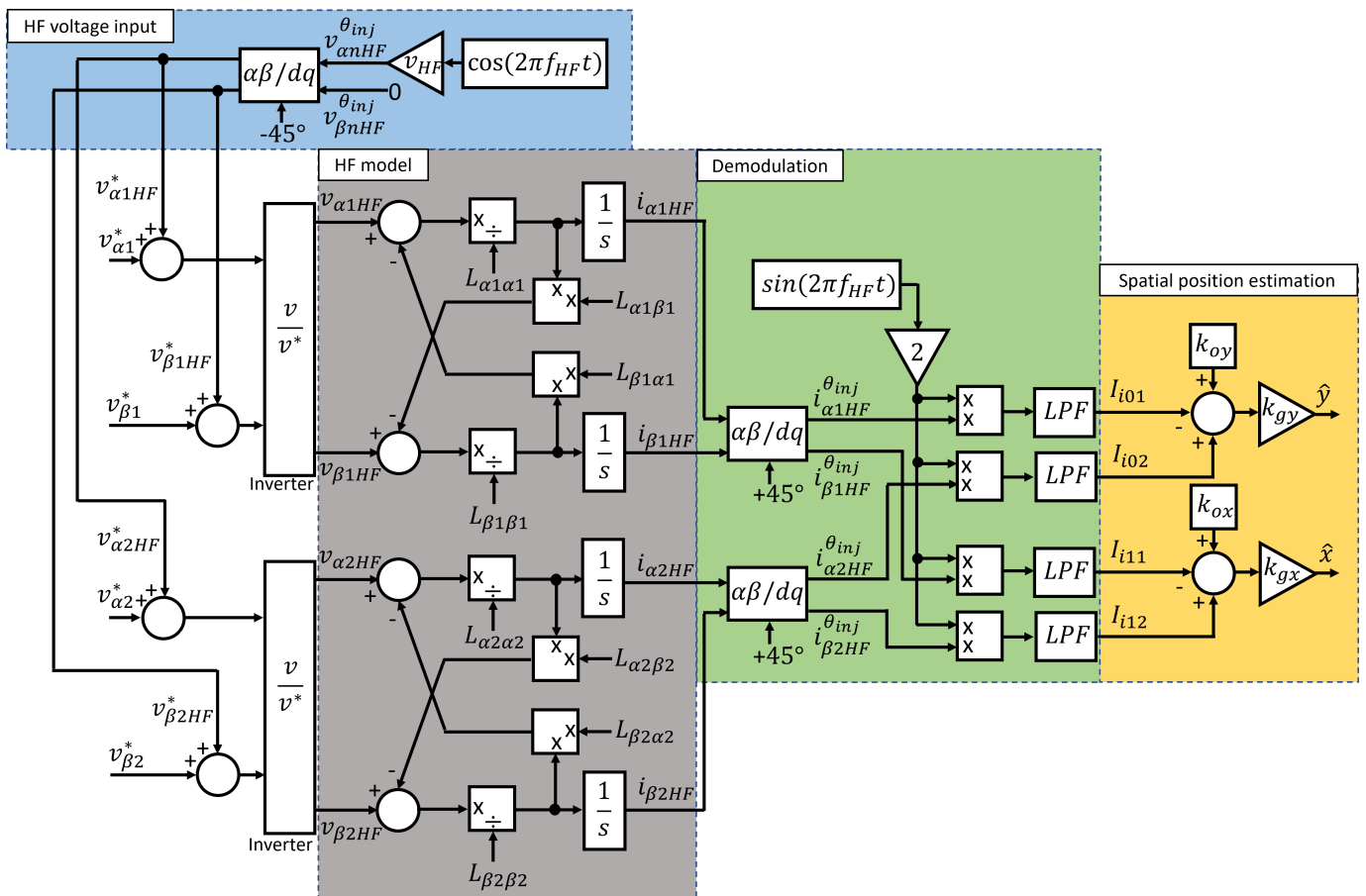

Figure 10. *xy*-position self-sensing block diagram, HF voltage injection in between $\alpha\beta$-axes (blue), HF model of the self-bearing machine (gray), HF current demodulation block diagram (green), and *xy*-position estimation block diagram (orange).

5. Experimental Results

This section shows the experimental results of the *xy*-position self-sensing algorithm. The experimental setup shown in Figure 11 is used. Figure 11a is the test self-bearing machine. To drive the test machine, two sets of 3-phase inverters with 6-current transducers are used, as shown in Figure 11b. The rotor is mechanically coupled with a DC machine that is fixed to the base, as shown in Figure 11b. The self-bearing machine stator is fixed to the *xyz*-mover of the position controlled linear motion stage. The linear motion stage shown in Figure 11c is position controlled by switched reluctance (SR) motors and drivers. The controlled position precision for *x*- and *y*-axes is 0.1 mm. The center position of the rotor with respect to the stator is position controlled by the linear motion stage, and used as an absolute position reference during the *xy*-position self-sensing experimentation.
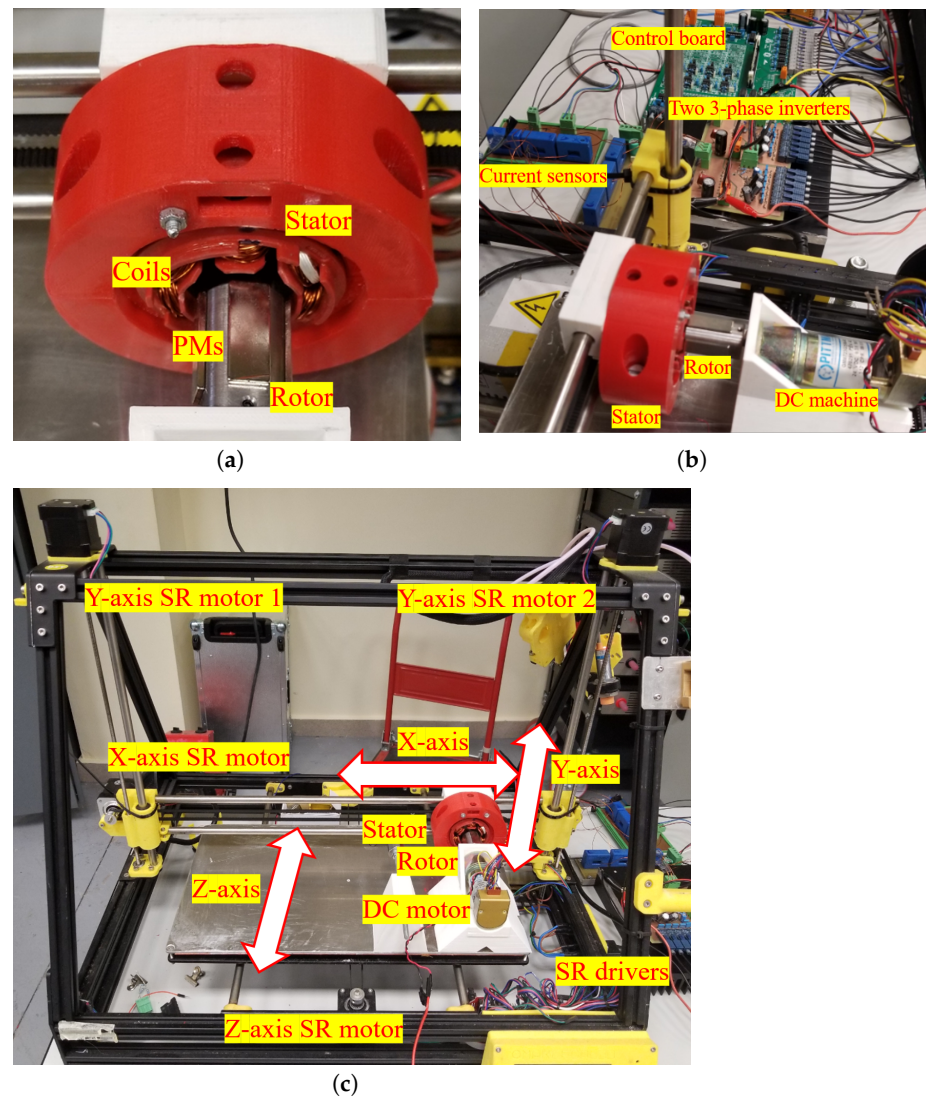
Figure 11. Experimental setup. (**a**) self-bearing machine; (**b**) self-bearing machine driver; (**c**) *xyz* linear motion stage.

The self-sensing experiment conditions are summarized in Table 4. Inverter DC link voltage is set to 40V. HF voltage ($v^*_{\alpha1HF}$, $v^*_{\beta1HF}$, $v^*_{\alpha2HF}$, and $v^*_{\beta2HF}$) shown in Figure 12a are injected. The resulting HF currents, when $x = 0$ mm and $y = -1$ mm, are shown in Figure 12b. Taking Park transformation at $+45°$, HF currents are measured. I_{i01}, I_{i11}, I_{i02}, and I_{i12} are shown in Figure 13a, which are obtained following demodulation procedure (green) shown in Figure 10. The pulsating HF current will result in pulsating HF torque and force that will not impact the average torque and force. Nevertheless, the HF injection condition, i.e., f_{HF} and V_{HF}, should be chosen carefully to minimize the interference between HF injection induced torque and force and the controlled torque and force. The f_{HF} is chosen as one-tenth of the switching frequency to minimize the impact of the switching voltage of PWM. The V_{HF} of <3% of the DC link voltage of the inverter can be selected for the proposed self-sensing algorithm. The proposed algorithm is tested in open-loop assuming that the voltage excitation results in minimal impact to the drive system in closed-loop. Finally, Figure 13b illustrates the estimated x and y positions, $\hat{x}$ and $\hat{y}$, using (39) and (40). Using 500 Hz bandwidth LPF, the estimated position converges to the steady state value in 2 ms. Steady state position estimation error was 4%, and peak to peak estimation error was $\pm8\%$ for maximum operating range of ±1 mm. The peak to peak error is due to a voltage synthesize error from PWM VSI. The position estimation bandwidth, which affects

position feedback control, is limited to LPF bandwidth. To achieve high bandwidth for the self-sensing, a higher PWM switching frequency should be used.

Table 4. *xy* self-bearing experimental conditions.

V_{DC}	40 [V]	k_{gx}	23.5
V_{HF}	0.015 [p.u.]	k_{ox}	0.0058
f_{HF}	1000 [Hz]	k_{gy}	23.5
LPF bandwidth	500 [Hz]	k_{oy}	−0.0006

To further show viability of the *xy*-position self-sensing, a series of experimental results on $\hat{x}$, $\hat{y}$ are shown in Figures 14 and 15. In Figure 14, the center of the rotor is held at constant *y*-positions while the *x*-positions are varied from −1 mm to 1 mm in incremental steps of 0.5 mm, see Figure 11c. Experimental conditions are summarized in Table 4. *xy*-position self-sensing block diagram shown in Figure 10 is used. Steady state value of demodulated HF currents and estimated $\hat{x}$-, $\hat{y}$-position are shown in Figure 14. It can be observed that I_{i11} and I_{i12} in Figure 14c,d are reverse-sensitive to the *x*-position variation while I_{i0n} in Figure 14a,b is insensitive. Using (39) and (40), $\hat{x}$ and $\hat{y}$ positions are estimated, simultaneously, and shown in Figure 14e,f. Figure 14g,h shows the estimation error.
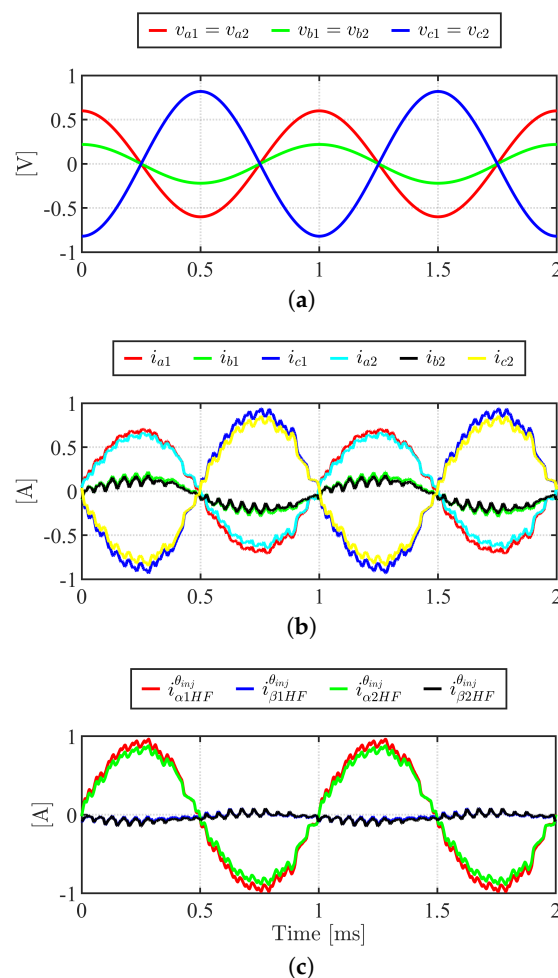

Figure 12. HF pulsating voltage injection and current response, $x = 0$ mm, $y = -1$ mm. (**a**) HF phase voltage command, abc_1 and abc_2; (**b**) HF phase current response, abc_1 and abc_2; (**c**) HF current response of $i_{\alpha1HF}^{\theta_{inj}}$, $i_{\beta1HF}^{\theta_{inj}}$, $i_{\alpha2HF}^{\theta_{inj}}$, and $i_{\beta2HF}^{\theta_{inj}}$.

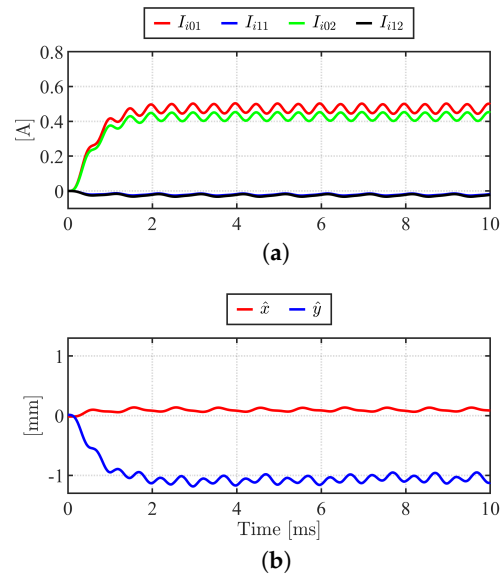**Figure 13.** *xy*-position estimation experimental results, $x = 0$ mm, $y = -1$ mm. (**a**) demodulated α and β HF current, I_{i01}, I_{i11}, I_{i02}, and I_{i12}; (**b**) estimated *xy*-position, $\hat{x}$ and $\hat{y}$.
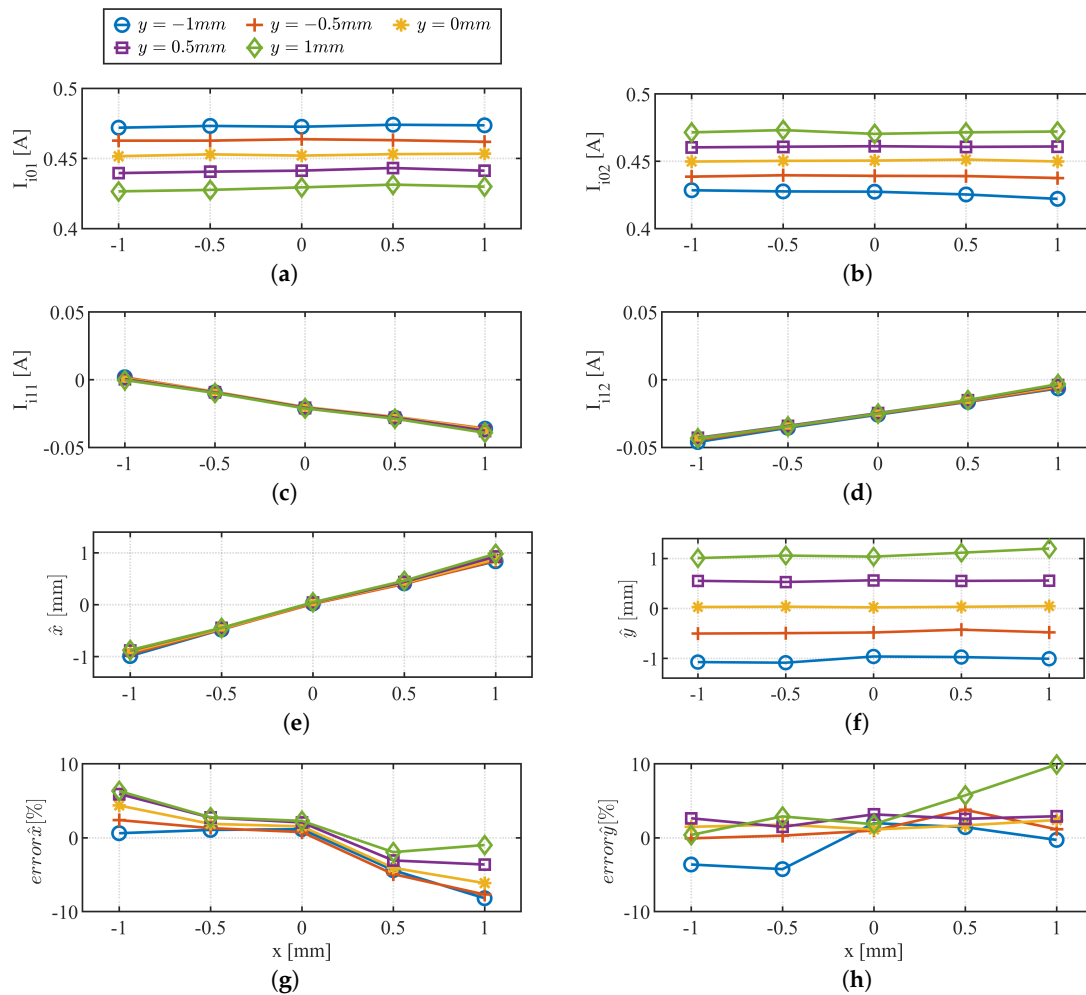

Figure 14. Experimental results varying *x* from −1 mm to +1 mm in steps of 0.5 mm at constant *y* position. (**a**) I_{i01}; (**b**) I_{i02}; (**c**) I_{i11}; (**d**) I_{i12}; (**e**) $\hat{x}$; (**f**) $\hat{y}$; (**g**) *error* $\hat{x}$; (**h**) *error* $\hat{y}$.
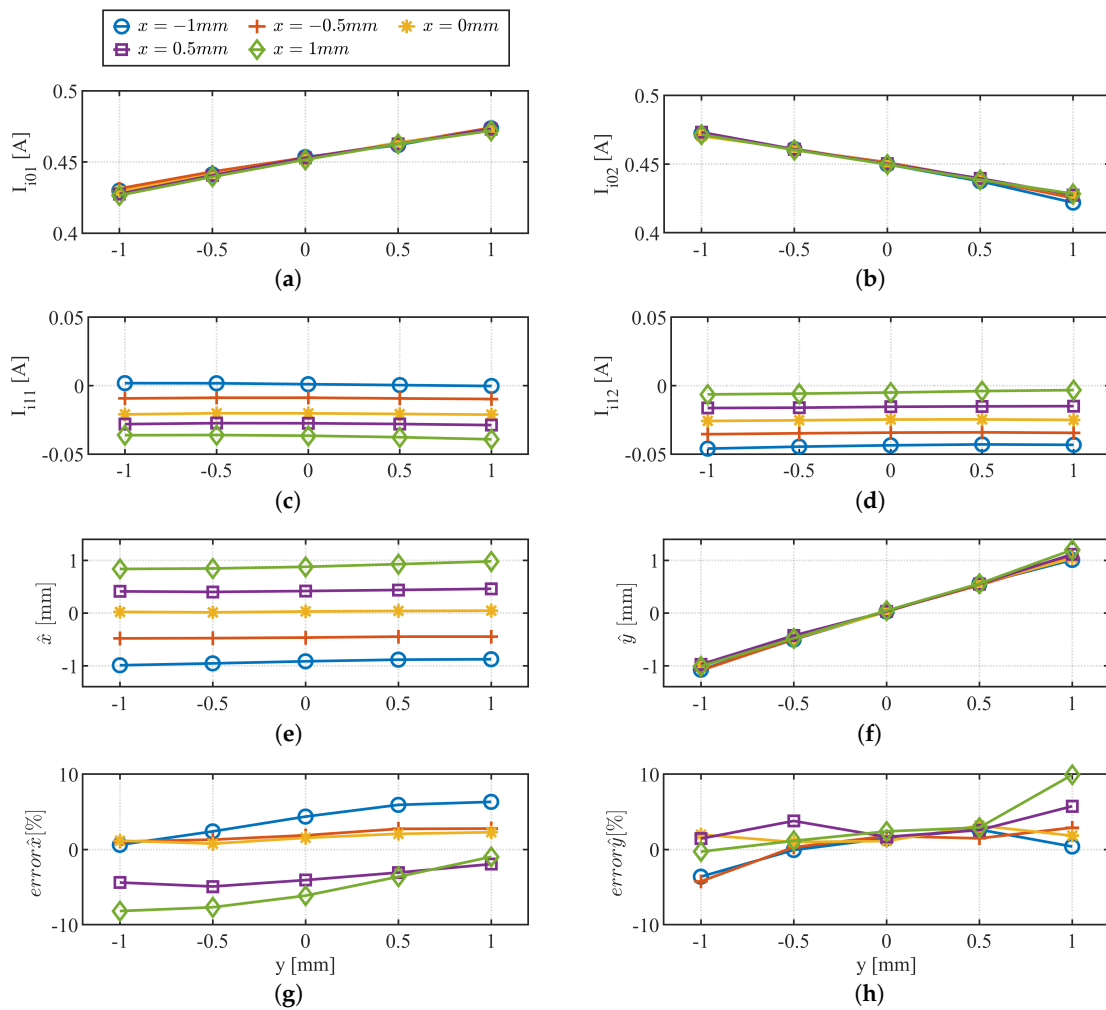
Figure 15. Experimental results varying y from +1 mm to −1 mm in steps of 0.5 mm at constant x position. (**a**) I_{i01}; (**b**) I_{i02}; (**c**) I_{i11}; (**d**) I_{i12}; (**e**) $\hat{x}$; (**f**) $\hat{y}$; (**g**) *error* $\hat{x}$; (**h**) *error* $\hat{y}$.

Figure 15 shows analogous results, but this time, the y-position is varied while holding the x-position constant. I_{i0n} is sensitive to the y position as expected in (37) and (38). The estimated x- and y-position results are shown in Figure 15e,f, respectively. Figure 15g,h shows the estimation error. The position estimation error increases as the rotor moves away from the center position due to other machine nonlinearity, e.g., magnetic saturation effect.

6. Conclusions

Rotor xy-position estimation based on the injection of an HF signal in combined winding self-bearing machines has been proposed. The proposed xy-position self-sensing algorithm does not require additional windings, e.g., suspension winding or search coils.

The model for machine inductances' sensitivities with respect to the xy-rotor position displacement are developed, based on the air-gap reluctance model, verified by FEA and experimental results. An HF pulsating voltage is injected between α- and β-axes to enable estimation of x- and y-rotor position, simultaneously utilizing both main- and cross-coupling inductance variation. The excitation frequency is carefully selected to minimize the interference to the closed-loop operation of the bearingless machine drive system. Demodulating the coupled HF current, $\hat{x}$ and $\hat{y}$ rotor positions are estimated. Experimental results have been provided to support the viability of the proposed technique.

References

1. Chiba, A.; Fukao, T.; Ichikawa, O.; Oshima, M.; Takemoto, M.; Dorrell, D.G. *Magnetic Bearings and Bearingless Drives*; Elsevier: Amsterdam, The Netherlands, 2005.
2. Sun, X.; Chen, L.; Yang, Z. Overview of Bearingless Permanent-Magnet Synchronous Motors. *IEEE Trans. Ind. Electron.* **2013**, *60*, 5528–5538. [CrossRef]
3. Gruber, W.; Rothböck, M.; Schöb, R.T. Design of a Novel Homopolar Bearingless Slice Motor With Reluctance Rotor. *IEEE Trans. Ind. Appl.* **2015**, *51*, 1456–1464. [CrossRef]
4. Ren, Z.; Stephens, L. Closed-loop performance of a six degree-of-freedom precision magnetic actuator. *IEEE/ASME Trans. Mechatron.* **2005**, *10*, 666–674. [CrossRef]
5. Severson, E.L.; Nilssen, R.; Undeland, T.; Mohan, N. Design of Dual Purpose No-Voltage Combined Windings for Bearingless Motors. *IEEE Trans. Ind. Appl.* **2017**, *53*, 4368–4379. [CrossRef]
6. Khamitov, A.; Gruber, W.; Bramerdorfer, G.; Severson, E.L. Comparison of Combined Winding Strategies for Radial Non-Salient Bearingless Machines. *IEEE Trans. Ind. Appl.* **2021**, *57*, 6856–6869. [CrossRef]
7. Kanebako, H.; Okada, Y. New design of hybrid-type self-bearing motor for small, high-speed spindle. *IEEE/ASME Trans. Mechatron.* **2003**, *8*, 111–119. [CrossRef]
8. Nguyen, Q.D.; Ueno, S. Modeling and Control of Salient-Pole Permanent Magnet Axial-Gap Self-Bearing Motor. *IEEE/ASME Trans. Mechatron.* **2011**, *16*, 518–526. [CrossRef]
9. Sugimoto, H.; Chiba, A. Parameter Identification of Current–Force Factor and Torque Constant in Single-Drive Bearingless Motors With Back EMF. *IEEE Trans. Ind. Appl.* **2019**, *55*, 4754–4761. [CrossRef]
10. Noh, M.; Gruber, W.; Trumper, D.L. Hysteresis Bearingless Slice Motors With Homopolar Flux-Biasing. *IEEE/ASME Trans. Mechatron.* **2017**, *22*, 2308–2318. [CrossRef]
11. Amrhein, W.; Gruber, W.; Bauer, W.; Reisinger, M. Magnetic Levitation Systems for Cost-Sensitive Applications—Some Design Aspects. *IEEE Trans. Ind. Appl.* **2016**, *52*, 3739–3752. [CrossRef]
12. Nian, H.; kang He, Y.; Huang, L.; Ying, H. Sensorless Operation of an Inset PM Bearingless Motor Implemented by the Combination Approach of MRAS and HF Signal Injection. In Proceedings of the 2006 6th World Congress on Intelligent Control and Automation, Dalian, China, 21–23 June 2006; Volume 2, pp. 8163–8167. [CrossRef]
13. Sivadasan, K.K. Analysis of self-sensing active magnetic bearings working on inductance measurement principle. *IEEE Trans. Magn.* **1996**, *32*, 329–334. [CrossRef]
14. Noh, M.D.; Maslen, E.H. Self-sensing magnetic bearings using parameter estimation. *IEEE Trans. Instrum. Meas.* **1997**, *46*, 45–50. [CrossRef]
15. Tsao, P.; Sanders, S.R.; Risk, G. A self-sensing homopolar magnetic bearing: Analysis and experimental results. In Proceedings of the Conference Record of the 1999 IEEE Industry Applications Conference, Thirty-Forth IAS Annual Meeting (Cat. No.99CH36370), Phoenix, AZ, USA, 3–7 October 1999; Volume 4, pp. 2560–2565. [CrossRef]
16. García, P.; Guerrero, J.M.; Briz, F.; Reigosa, D.D. Sensorless Control of Three-Pole Active Magnetic Bearings Using Saliency-Tracking-Based Methods. *IEEE Trans. Ind. Appl.* **2010**, *46*, 1476–1484. [CrossRef]
17. Tera, T.; Yamauchi, Y.; Chiba, A.; Fukao, T.; Rahman, M.A. Performances of bearingless and sensorless induction motor drive based on mutual inductances and rotor displacements estimation. *IEEE Trans. Ind. Electron.* **2006**, *53*, 187–194. [CrossRef]
18. Nian, H.; He, Y.; Chen, D.; Huang, L. Self-sensing of the rotor position and displacement for an inset permanent magnet type bearingless motor. In Proceedings of the 2007 International Conference on Electrical Machines and Systems (ICEMS), Seoul, Republic of Korea, 8–11 October 2007; pp. 1508–1512.
19. Chiba, A.; Santisteban, J.A. A PWM harmonics elimination method in simultaneous estimation of magnetic field and displacements in bearingless induction motors. In Proceedings of the 2011 IEEE International Electric Machines & Drives Conference (IEMDC), Niagara Falls, ON, Canada, 15–18 May 2011; pp. 1042–1047. [CrossRef]
20. Tsukada, N.; Onaka, T.; Asama, J.; Chiba, A.; Fukao, T. Novel Coil Arrangement of an Integrated Displacement Sensor with Reduced Influence of Suspension Fluxes for a Wide Gap Bearingless Motor. *IEEE Trans. Ind. Appl.* **2010**, *46*, 2304–2310. [CrossRef]

21. Kang, Y.G.; Fernandez, D. Self-Bearing Machine Modeling Reflecting Rotor Position Induced Non-Linearity Based on 7-D Lookup Table. *IEEE Trans. Magn.* **2021**, *57*, 8107910. [CrossRef]
22. Krause, P.C.; Wasynczuk, O.; Sudhoff, S.D.; Pekarek, S. *Analysis of Electric Machinery and Drive Systems*; Wiley Online Library: 2002; Volume 2. Available online: https://ieeexplore.ieee.org/book/6712180 (accessed on 30 November 2022).
23. Kang, Y.G.; Lorenz, R.D. Using Intentional Magnetic Saturation for HFI Based Self-Sensing with SPMSMs. In Proceedings of the 2018 IEEE International Conference on Power Electronics, Drives and Energy Systems (PEDES), Chennai, India, 18–21 December 2018; pp. 1–6. [CrossRef]
24. Kang, Y.G.; Reigosa, D.; Sarlioglu, B.; Lorenz, R. D and q-axes Inductance Estimation and Self-Sensing Condition Monitoring using 45 Angle High-Frequency Injection. *IEEE Trans. Ind. Appl.* **2020**, *57*, 506–515. [CrossRef]